Optical Detection of Single Nanoparticles and Viruses

Filipp V. Ignatovich, David Topham, and Lukas Novotny

(Invited Paper)

***Abstract*—We have developed two different optical techniques for the detection of nanoscale particles. One of the methods is based on measuring the optical gradient force exerted on a nanoparticle as it passes through a confined optical field, and the other method uses a background-free interferometric scheme to detect the scattered field amplitude from a laser-irradiated particle. In both cases, the measured signal depends on the third power of the particle size (R^3) as opposed to the R^6 dependence inherent to traditional scattering-based detection methods. The weaker size dependence in our schemes leads to a better signal-to-noise ratio (SNR) for small particles. Similar to mass spectrometry, the first detection method influences the trajectory of a particle as it passes through a tightly focused laser beam. On the other hand, the second detection method combines an interferometer with a split detector that yields no signal in the absence of a particle. For both systems, we demonstrate real-time (1 ms) detection of single nanoparticles in a microfluidic system and discuss the limits of each detection approach.**

***Index Terms*—Interferometry, nanoparticles, optical gradient force, optical tweezers, quadrant photodetector, sensor, viruses.**

I. Introduction

THERE is a high demand for sensors that are able to detect small amounts of pathogenic biological agents in public areas or in field conditions [1], [2]. Because of the devastating potential for rapid infection from a small amount of biological agents, biological weapons are likely candidates for future terrorist attacks. Recent events have witnessed the danger of biological agents. Examples are anthrax spores used to disrupt the U.S. government, the SARS outbreak and associated problems with its containment, and the recent bird flu pandemic. Viruses [3] are especially dangerous because of the high infectivity, small size, and no existing cures [4]. Early detection is a key defense against this threat. Therefore, a broad network of sensors has to be deployed. These sensors must be affordable and sufficiently robust to be installed in public spaces, such as transit systems, food industries, water treatment plants, distribution systems, or mail delivery systems. Most viruses have a characteristic size in the range of 20–200 nm [5]. Because of this small size, viruses are extremely challenging to detect in real time. Most existing detection schemes for viral biomolecules rely on biochemical binding to functionalized surfaces. The inherent complexity of these techniques, as well as their cost and difficult maintenance, are limiting factors for their widespread deployment.

Manuscript received December 10, 2005; revised September 15, 2006.

F. V. Ignatovich and L. Novotny are with the Institute of Optics, University of Rochester, Rochester, NY 14627 USA (e-mail: filipp@nanooptics.org; novotny@optics.rochester.edu).

D. Topham is with the David H. Smith Center for Vaccine Biology and Immubnology, University of Rochester Medical Center, Rochester, NY 14642 USA (e-mail: david_topham@urmc.rochester.edu).

Digital Object Identifier 10.1109/JSTQE.2006.885086

Nanoparticle detection is not only important for biodefence but also for a broad range of applications in other fields. For example, semiconductor nanoparticles are used as single photon emitters in quantum information science [6] and as fluorescent markers for biological processes [7]. Similarly, noble metal particles are used as contrast agents in microscopy [8], as biochemical sensors [9], as probes in scanning probe microscopy [10], or as nonbleachable biological labels [11]. Furthermore, specially engineered particles such as nanoshells are employed for photothermal tumor ablation and for cancer therapies [12]. Polymer nanoparticles are used as calibration standards and, in functionalized form, also as probes in biological imaging [13]. Therefore, the ability to detect and characterize single nanoparticles is beneficial for a broad range of applications.

Among alternative detection strategies, *optical* techniques are especially attractive because of their noninvasive nature, high sensitivity [14], and potential for real-time detection [15]. Optical methods seem to be favorable for reasons of fastness, simple implementation, and low maintenance. There have been attempts to optically detect nanoparticles by indirect means, for example, by fluorescent labeling of particles or biological species [16]. While fluorescently labeled particles are easy to detect, the size information is not readily available. Other strategies include immobilization on a surface and subsequent analysis with dark field microscopy [17] or by scanning probe techniques, such as scanning near-field optical microscopy [18]. While these approaches succeeded in detecting small particles, they cannot be applied *in vitro* and in real time.

The field of real-time optical particle detection is well developed, with many detectors currently available in the market. Most commonly, optical methods for particle detection rely on light scattering [19]. Light scattering measurements are very sensitive to small changes in particle size and optical properties. In the simplest version, these so-called optical particle counters (OPCs) [20], [21] consist of a light source (usually a laser) that illuminates a sample volume of an aerosol or a liquid flow containing particles of interest. An off-axis detector collects the scattered light. The latter is a function of particle properties such as size, concentration, and optical density. However, current OPCs lack the sensitivity to detect individual nanoscale particles.

There are many variations of OPCs, some of which count individual particles, such as the flow cytometer [22], the phase Doppler anemometer(PDA) [23], localized dynamic light scattering (LDLS) [24], [25], and some versions of condensation nuclei counters (CNC) [26]. Other OPCs measure ensemble averages. Examples are dynamic light scattering (DLS) [27], nephelometers (or multiangle photometer) [28], and other versions of CNCs [26]. While DLS and CNC are capable of detecting and characterizing ensembles of small nanoparticles, single

particle counters are not sufficiently sensitive to detect particles smaller than 200 nm in size. OPCs collect and measure the *power* of scattered light, which yields a sixth power dependence on particle size (R^6), where R is the particle radius. While the R^6 dependence is beneficial in discriminating particles of similar dimensions, the signal-to-noise ratio (SNR) rapidly deteriorates as the target particles become smaller, rendering such particles indiscernible from background noise.

It is, therefore, intuitive to assume that an interaction mechanism with a weaker particle size dependence may significantly boost the SNR when detecting small particles. Such mechanisms have been explored before. One strategy relies on detecting the scattered light interferometrically thereby accessing the scattered electric field amplitude as opposed to the scattered power. This approach has been demonstrated almost 20 years ago, in a patent by IBM [29], [30] and recently applied for the detection of immobilized gold particles as small as 5 nm in diameter [14]. Another detection scheme with a R^3 signal dependence relies on measuring particle absorption cross sections by means of the photothermal effect [31]. Although these methods extend the detection sensitivity to smaller particle sizes, they are not suited for real-time nanoparticle detection.

In the following sections, we describe two methods that were developed to detect single particles with sizes smaller than 100 nm in radius. Both methods feature a R^3 signal dependence and are able to detect single virions in aqueous environments. The first method, making use of optical gradient forces, is described in Section II. The second method, described in Section III, relies on measuring the scattered electric field using an interferometer and a split photodetector. The latter ensures background-free detection similar to single molecule fluorescence measurements.

II. Optical Gradient Force

The invention of optical tweezers [32], [33] made it possible to manipulate matter with forces in the pico-newton range [34]. The force is generated by the field gradient near the focus of a strongly converging laser beam. For dielectric materials, the force is directed toward the center of the focus, thereby preventing a trapped object from escaping. For particles much smaller than the wavelength of the trapping laser (Rayleigh limit), the force is given by [35]

$$\mathbf{F}_0 = \frac{\alpha'}{2}\nabla|\mathbf{E}(\mathbf{r}_0)|^2 \tag{1}$$

where α' is the real part of the particle polarizability and $\mathbf{E}(\mathbf{r}_0)$ is the root-mean-square value of the time-dependent electric field vector at the location $\mathbf{r}_0$ of the particle. The polarizability of a spherical particle with dielectric permittivity ε_p surrounded by a medium (water, air, vacuum) with dielectric permittivity ε_s is given by

$$\alpha = 4\pi R^3 \varepsilon_0 \varepsilon_s \frac{\varepsilon_p - \varepsilon_s}{\varepsilon_p + 2\varepsilon_s} \tag{2}$$

where R is the particle radius. Unlike light scattering, the gradient force $\mathbf{F}_0$ scales with the third power of the particle size (R^3 versus R^6).

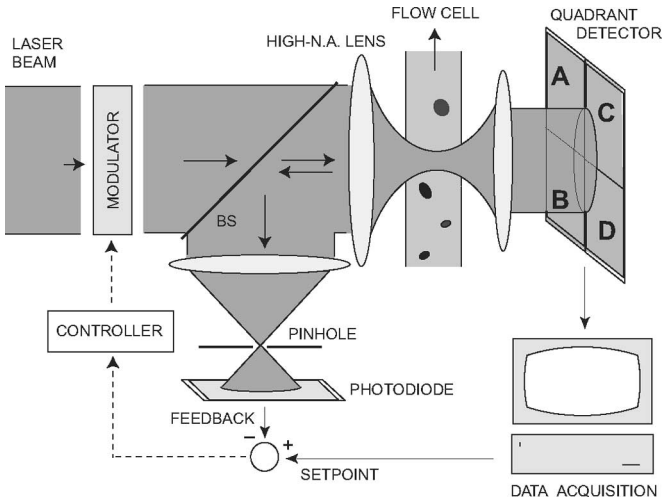

Fig. 1. Experimental configuration for the optical gradient force detection.

Here, we consider particles carried by a viscous fluid (i.e., water) through a laser focus. As a single particle approaches the laser focus, the optical gradient force (1) pulls the particle toward the focus thereby accelerating it. Once the particle passes through the focus, it is pulled back giving rise to deceleration. Consequently, the laser focus influences the velocity trajectory of the particle. At any instant of time, the Stokes force experienced by the particle is calculated as

$$\mathbf{F}_s = 6\pi\eta R(\mathbf{v}_p - \mathbf{v}_m) \tag{3}$$

where η is the viscosity of the medium, and $\mathbf{v}_p, \mathbf{v}_m$ are the velocities of the particle and medium, respectively. The motion of a particle in a viscous fluid is overdamped and, hence, the Stokes force and the gradient force are equal, i.e.,

$$\mathbf{v}_p = \mathbf{v}_m + \frac{\mathbf{F}_0}{6\pi\eta R}. \tag{4}$$

Because $\mathbf{F}_0$ changes sign as the particle passes through the focus, (4) demonstrates that a particle moving toward the laser focus is accelerated, i.e., it moves faster than the liquid. However, once the particle crosses the focus, it is slowed down and the resulting velocity trajectory of the particle is nonuniform. The trajectory is characterized by different amounts of time it takes for the particle to move toward the focus and away from the focus. The difference in these times depends on the particle size. The larger the particle, the stronger the optical force, and the larger the time difference will be. Our force detection method is based on measuring this time difference by tracking the particle position as it passes through the laser focus.

The detector configuration is schematically shown in Fig. 1. An incoming laser beam is tightly focused with a microscope objective into a nanofluidic channel that transports a solution with nanoscale particles. The particles are carried through the focus at constant velocity by the use of electro-osmosis. The optical force perturbs the trajectory of the particles. A second objective, placed on the opposite side, is used to collect the scattered and transmitted light. The particle position relative to the laser focus is monitored in real time with a quadrant detector placed behind the collecting objective. To prevent larger

particles from being trapped in the laser focus, a feedback loop automatically attenuates the laser power when the backscattered light intensity exceeds a threshold value.

The idea of using a quadrant detector to monitor the particle motility in the focus of a microscope objective is well established. It was first introduced by Gittes and Schmidt [36], and found various applications, such as the measurement of pico-newton forces in biophysical experiments [37], [38]. The techniques of position tracking is based on combining the light scattered by the particle with the transmitted laser light, thereby creating an interferometric pattern in the detector plane. The weighted intensity center of the interference pattern depends on the particle's relative position with respect to the focus. Therefore, the signal difference between two halves of the photodetector is a direct measure of the particle's coordinates. The latter can be calculated as [39]

$$\Delta x = \frac{\pi\,\alpha_p}{2\varepsilon_0\lambda^3}\,\cos[\arctan(y_0/x_0)]\int_0^{\theta\max}\exp(-k^2w_0^2\theta^2/4) \times \cos(kz_0\cos\theta)J_1\left(k\sqrt{x_0^2+y_0^2}\,\sin\theta\right)\theta\,d\theta \tag{5}$$

$$\Delta y = \frac{\pi\,\alpha_p}{2\varepsilon_0\lambda^3}\,\sin[\arctan(y_0/x_0)]\int_0^{\theta\max}\exp(-k^2w_0^2\theta^2/4) \times \cos(kz_0\cos\theta)J_1\left(k\sqrt{x_0^2+y_0^2}\,\sin\theta\right)\theta\,d\theta \tag{6}$$

where α_p is the particle's polarizability, λ is the wavelength of the laser, x_0, y_0, and z_0 are the particle's coordinates [assuming a focus at $(0,0,0)$], ω_0 is the beam waist radius, and J_1 is the first-order Bessel function. The integration is done over the collection angle θ, with $\theta_{\max}$ being the maximum collection angle defined by the numerical aperture of the collecting objective. The detector is positioned in a way that the transmitted laser beam (in the absence of any particles) is centered on the quadrant detector that gives rise to a zero detector signal. If a particle is located on the optical axis $(x_0 = y_0 = 0)$, the detector signal is also zero because the symmetry with respect to the detector center is preserved. For other particle positions, the detector signal is nonzero. For more details, the interested reader is referred to [39].

To illustrate the detection principle, let us assume that the particle is moving with a constant velocity along the x-axis $(y_0 = 0)$ in the focal plane $(z_0 = 0)$. The calculated temporal detector signal according to (5) is shown in Fig. 2. It consists of a peak and a valley. In between, when the signal reaches a zero value, the particle crosses through the center of the laser focus. For a given laser power, only particles for which the optical force is negligible exhibit a symmetric temporal signal. This is because the particle trajectory remains unperturbed and the particle's velocity stays constant.

Fig. 2 shows the calculated signal for two polystyrene beads of different radii, 50 and 100 nm. The chosen parameters are close to the actual experimental values ($v_m = 500$ μm/s, NA $= 1.4$, laser wavelength λ is 532 nm, laser power is 200 mW). Because the focused laser field exerts a stronger force on large particles, it is evident that the signal of the larger particle is more distorted

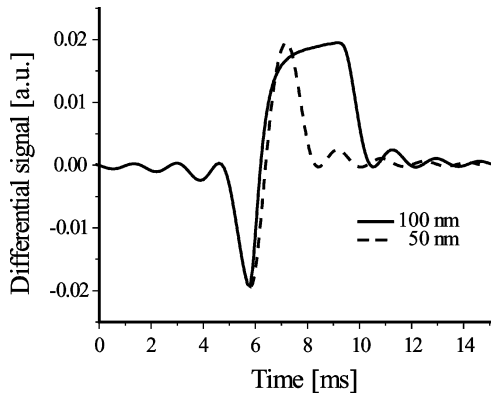

Fig. 2. Simulated time traces for two different particle sizes. A typical trace consists of a valley followed by a peak. A large particle experiences a strong gradient force resulting in an asymmetrical trace. For a small particle, the signal remains symmetric, i.e., the valley is a mirror image of the peak. The degree of the signal asymmetry is used as a measure for the optical force and, hence, for the particle polarizability. The degree of the asymmetry is calculated using the ratio between the widths of peak and valley and is denoted as *force parameter*. In the figure, the signal of the smaller particle has been scaled by a factor of 8.

than the signal of the smaller particle. The large particle moves faster when it approaches the focus and slower when it moves away from focus. Consequently, the temporal width (FWHM) of the valley (t_1) and the temporal width of the peak (t_2) of the curve are not the same and their ratio is a measure for the optical force magnitude and, thus, the particle polarizability. For the following, we shall denote the ratio

$$R_p = \frac{t_2}{t_1} \tag{7}$$

as a force parameter.

The experimental setup of our force-based nanoparticle sensor is schematically depicted in Fig. 1. After passing through a single-mode fiber, the light from a 532 nm laser (Coherent Inc., Santa Clara, CA) is collimated and sent into an inverted microscope (TE300, Nikon, Japan). A high numerical aperture objective (NA $= 1.4$, PlanApo, $60\times$) is used to tightly focus the laser beam into a flow-cell. The transmitted beam and the light scattered from the individual particles passing by is collected by an objective $(\mathrm{NA} = 0.85)$. The back aperture of the collimating objective is imaged by a lens onto a quadrant detector (SPOT 9DMI, UDT Sensors, Hawthorne, CA). In order to extend the detection capabilities of our sensor to a broader range of particle sizes, we implemented a feedback loop that attenuates the laser power when the backscattered light from a larger particle exceeds a given threshold [39]. In our experiment, however, the feedback is deactivated in order to ease the analysis and discussion.

The flow-cells were fabricated at the Cornell Nanofabrication Facility. Details of the fabrication process can be found in [15]. It is worth noting here that the channels are designed to have dimensions comparable to the laser focus. In a flow-cell with dimensions considerably larger than the laser focus, large particles passing at some distance from the focus experience the same force as small particles passing exactly through the center of the focus. In order to reduce or even eliminate this uncertainty, we have fabricated an array of nanochannels with the dimensions of

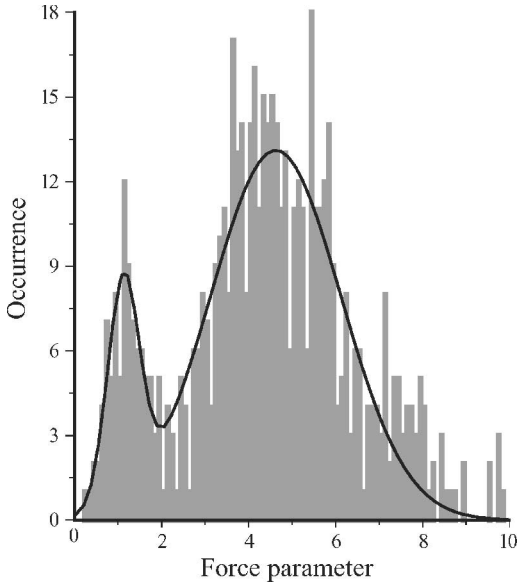

Fig. 3. Histogram of the force parameter for a solution consisting of a mixture of 50- and 100-nm polystyrene beads. The two peaks in the distribution indicate that the different-sized particles can be distinguished from each other on an individual particle basis. The *left peak* corresponds to 50-nm particles and the *right peak* corresponds to 100-nm particles. The large width of the distribution is due to the Brownian motion that affects the total force acting on the particle as it passes through the focus.

only 500 nm. The 15-μm-long nanochannels are connected to an array of larger flow-cells between pairs of reservoirs separated by a distance of 30 mm. The liquid flow inside the channels is generated by electro-osmosis [40]. A 10-V potential applied to the gold electrodes immersed in the reservoirs results in a fluid flow velocity of $\approx$500 μm/s. The time resolution of this method is given by the amount of time it takes a single particle to cross the laser focus, which is approximately 1 ms.

Factory prepared bead solutions (polystyrene $R = 50$-nm and $R = 100$-nm beads from Polysciences Inc., with a specified coefficient of variance of 5%) were diluted by adding deionized water to achieve desired particle concentrations (10^{10} to 10^{11} particles/ml) and then mixed together. Tween-20 surfactant (0.02% by volume) was added to the solution to prevent the particles from clustering. At 10^{11} particle/ml, there are about ten particles crossing the laser focus in a second. Therefore, the probability of two or more particles appearing in the laser focus within the same millisecond is very small. It is further reduced by the presence of the surfactant, which keeps the particles separated.

Fig. 3 shows the recorded histogram of the force parameter for a mixture of 50- and 100-nm polystyrene beads. The two separated peaks prove the ability of the sensor to distinguish particles of different sizes by making use of the optical gradient forces. The large width of the peaks indicates, however, a considerable measurement error. While the size of the nanochannels partially contributes to the measurement error as described earlier, the force measurement itself is not background-free. Brownian motion has a strong influence on the total force acting on a particle. It influences the amount of time a particle spends in opposite halves of the focus, which, in turn, affects the temporal symmetry of the measured quadrant detector signal. This is especially true for large particles, as Brownian motion prevents short-term trapping events to be distinguished from the desired slowing down process. In stationary optical tweezers, Brownian motion kicks a particle out of the optical trap. On the other hand, it is also capable of the reverse action, i.e., of keeping the particle trapped in the presence of external forces such as liquid flow. In this case, the particle spends more time in the focus than in the one predicted by an equation of motion defined only by optical and Stokes forces. For instance, this is the reason for the asymmetric distribution of the force parameter for 100 nm particles.

The effective recognition of particles of different sizes demands that the force parameter distributions do not overlap. Laser power and liquid speed can be tailored in order to achieve sufficient separation between individual distributions. Increasing the laser power moves the force parameter for a given particle size to higher values; however, it also results in an increased width of the distribution. Increasing the laser power slows the particles down and, hence, increases the influence of the Brownian motion. On the other hand, increasing the liquid speed reduces the overall time the particle spends in the focus, thus reducing the effect of the Brownian motion on the force parameter distribution. However, at the same time, it reduces the relative perturbative effect of the optical force, thereby reducing the asymmetry of the measured quadrant detector signal. Only a simultaneous increase of the laser power and liquid speed can reduce the distribution width, while keeping the force parameter distributions sufficiently separated [15].

The maximum values of the laser power and liquid speed are, however, limited. A high liquid speed requires a large quadrant detection bandwidth, thus increasing the electronic noise and reducing the SNR. A high laser power, on the other hand, may affect the structural properties of the particles of interest through electrostriction or thermal effects. The force detection approach, while promising, cannot be considered practical due to the strong influence of the Brownian motion. Therefore, a second approach was pursued, as described in the following section.

III. Interferometric Detection

In this section, we describe a *background-free* detection approach, based on the interferometric measurements of the scattered field *amplitude*. As mentioned earlier, the idea of detecting the scattered field as opposed to the scattered power has been around for some time; however, the extension to the background-free detection has been introduced only recently [41]. This approach leads to the unsurpassed real-time detection sensitivity for low-index particles such as individual viruses in aqueous solution.

The experimental setup is schematically shown in Fig. 4. It shares some common parts with the setup described in the previous section. A laser beam ($\lambda = 532$ nm; Coherent Compass 315M-100) is split by a $50/50$ beamsplitter into two perpendicular paths, thus creating two arms of a Michelson interferometer. The beam in one arm is focused by an oil-immersion objective $(60\times, \mathrm{NA} = 1.4)$ into the fluidic nanochannel. A solution with particles of interest is transported through the channel using electro-osmosis with the speed of approximately 500 μm/s,

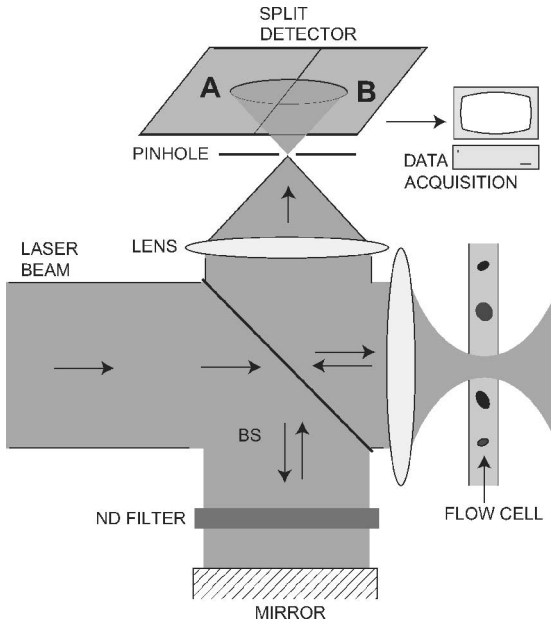

Fig. 4. Experimental configuration used to interferometrically detect single nanoparticles. A laser beam is tightly focused into a nanofluidic channel. Particles or viruses are carried through the focus by electro-osmotic flow. Scattered light from the individual particles passing through the laser focus is collected by the focusing objective, then recombined with a reference beam and directed onto a split photodetector. The differential signal from the photodetector is proportional to the scattered field amplitude and, therefore, to the third power of the particle size.

thus making the interferometric method comparable to the optical force approach in terms of time resolution. The particles used to test the interferometric approach include 25(10)-, 50(5)-, 100(5)-, and 175(4)-nm radius polystyrene beads from Polyscience, Inc.; 15(n/a)- and 50(4)-nm polystyrene beads from Duke Scientific; and 7(8)- and 20(8)-nm gold beads from Ted Pella, Inc. (Numbers in parentheses specify the variance.)

The backscattered light from the particle passing through the laser focus is collected with the focusing objective, and recombined with the reference beam at the beamsplitter and directed onto a split photodetector. The power of the reference beam can be arbitrarily attenuated using a $\lambda/2$ plate placed between two polarizers.

The SNR in this detection scheme depends sensitively on the use of a split photodetector and the ability to attenuate the reference beam intensity. The split detector assumes a function similar to the position detector described in the previous section, but with one main difference. In the position-sensing configuration, the scattered light is recombined with the transmitted laser light that cannot be independently attenuated. In the interferometric detection configuration, the reference beam intensity can be adjusted to tailor the SNR, as detailed later.

Let us denote the scattered field as E_s and the reference field as E_r. The intensity distribution on the detector surface is then given by

$$I = |\boldsymbol{E}_r|^2 + |\boldsymbol{E}_s|^2 + 2Re(\boldsymbol{E}_r^* \boldsymbol{E}_s). \tag{8}$$

The signal from the detector is calculated by taking the difference between the opposite halves of the detector and normalizing it to the total incident power, i.e.,

$$S = \frac{\int_{\subset} I\, da - \int_{\supset} I\, da}{\int_{\circ} I\, da} \tag{9}$$

where $\subset$ denotes integration over one half of the photodetector surface, $\supset$ over the opposite half, and $\circ$ over the full detector surface area.

In the absence of the scattered light, the laser spot is positioned at the center of the photodetector. Therefore, $\int_{\subset} E_r^2\, da = \int_{\supset} E_r^2\, da$ and the differential signal (9) is zero. When a nanoparticle moves through the laser focus it scatters light and, hence, the differential signal becomes the interferometric term

$$S = 2\,\mathrm{Re}\left\{ \frac{\int_{\subset} \boldsymbol{E}_r^* \boldsymbol{E}_s\, da - \int_{\supset} \boldsymbol{E}_r^* \boldsymbol{E}_s\, da}{\int_{\circ} |\boldsymbol{E}_r|^2\, da} \right\} \tag{10}$$

where we have neglected the scattered light intensity term $|\boldsymbol{E}_s|^2$ in the numerator, because it is much smaller than the other terms. In the denominator, we account only for the most dominant term, the reference beam intensity $|\boldsymbol{E}_r|^2$. The amount of the scattered light from the particle depends on the particle's position with respect to the focus. Therefore, the signal from the split photodetector varies in time as the particle travels through the focus, similar to that in Fig. 2. Assuming that all particles travel approximately along the same path, the amplitude of the resulting signal will be the same for the particles of equal size.

For a given instant of time, the signal $S(t)$ in (10) depends linearly on the electric field amplitude E_s of the scattered light. On the other hand, the scattered field is linearly related to the amplitude of the focused laser field E_f and to the particle polarizability α. Hence, the detector signal satisfies the proportionality

$$S(t) \propto \alpha' \sqrt{P_f / P_r} \tag{11}$$

where P_f and P_r are the powers of the focused laser beam and the reference beam, respectively. The proportionality constant depends on various experimental parameters such as numerical aperture of the objective, mirror reflectivity, detector quantum efficiency, physical constants, result of spatial integrations, and particle position with respect to the focus and, therefore, on time. Contrary to the position-sensing configuration in Section II, P_f and P_r are independent of each other. Thus, the total incident laser power can be increased and focused to a more intense spot while the reference beam can be attenuated independently or simultaneously, thus increasing the amplitude of the differential signal $S(t)$.

In order for the SNR to increase as the signal amplitude is enlarged, the noise level has to stay unchanged. The differential signal noise is defined by the detector noise in the absence of the scattered field. Since the spot of the reference beam is positioned in the center of the split photodetector, the signal noise does not depend on the power noise of the laser. This, and the fact that the differential signal is zero in the absence of the particle, makes this detection scheme very sensitive. The main source of noise in our interferometric detection scheme is the laser beam pointing instability and the electronic noise associated with the photocurrent-to-voltage conversion. The pointing

instability causes the beam spot to deviate from its central position, giving rise to a nonzero detector response. The noise level for a differential signal can be expressed as

$$N = \sqrt{P_v^2 + [\theta_{\rm rms} P_r]^2} \,/\, P_r \tag{12}$$

where P_v represents the "power equivalent" of the electronic detector noise, and $\theta_{\rm rms}$ is the root-mean-square of the angular pointing instability of the laser. Equation (12) predicts that when $P_r \gg P_v$, the noise becomes constant and proportional to $\theta_{\rm rms}$. However, when P_r is attenuated such that $\theta_{\rm rms} P_r \lesssim P_v$, the noise level increases rapidly with decreasing P_r. Using (11) and (12), we obtain

$$\frac{S}{N} \propto \alpha' \sqrt{\frac{P_f P_r}{P_v^2 + [\theta_{\rm rms} P_r]^2}} \tag{13}$$

which predicts that the best SNR is achieved when the power of the reference beam is $P_r^{\max} = P_v \,/\, \theta_{\rm rms}$, and the maximum SNR is given by

$$\frac{S}{N}_{\max} \propto \alpha' \sqrt{\frac{P_f}{P_v \theta_{\rm rms}}}. \tag{14}$$

As expected, reducing the electronic noise and the beam pointing stability increases the maximum SNR. If P_v and $\theta_{\rm rms}$ are adjusted to the lowest possible values, the recipe for achieving the best sensitivity and the lowest detection limit is to increase the laser power while keeping the reference beam at the level of the maximum SNR.

The lowest possible reference beam power is, however, determined by the backscattered light in the absence of a passing particle. This backscattered light is due to the optical index mismatch between different interfaces and is analogous to the background fluorescence in single molecule experiments. Because this backscattered light interferes with the scattered light from a passing particle, it assumes a function similar to the reference beam. While increasing the sample arm beam intensity P_f, this unwanted backscattering may become stronger than the reference beam power. However, the index mismatch between interfaces can be minimized in a favorably engineered sensor design.

Fig. 5 shows the recorded signal distribution for a mixture of particles with four different sizes. The particles appear to be well resolved and the widths of the distributions are consistent with the actual particle size distributions according to the supplier. Fig. 6(a) and (b) contains distributions for the smallest single particle we can currently detect with an SNR value of 3.

Fig. 7 shows the signal distribution for a mixture of $R = 50$ nm and $R = 100$ nm particles, the same mixture as used before for the gradient force based approach (cf., Fig. 3). A comparison between the two distributions confirms that the interferometric approach is more sensitive and possesses a better resolving power than does the optical force approach. Compared to the gradient force approach, the interferometric method is not affected by the Brownian motion, because it is based on measuring the *maximum* scattering amplitude. Brownian motion affects the time at which the maximum occurs but not the value of the maximum. The lateral confinement provided by the channel as well as the linear motion provided by the electro-osmotic flow ensure that every particle passes through the laser focus. The interferometric approach yields distributions that are much narrower and better separated. The finite width of the individual particle distributions originates from the nonuniform intensity distributions in the nanochannels as well as the actual size distribution of the particles. Therefore, despite the clear advantage of the interferometric approach, the acquired distributions are still wider than the factory specifications. Narrower distributions can be achieved by further reducing the dimensions of the nanochannels or by increasing the focal spot size.

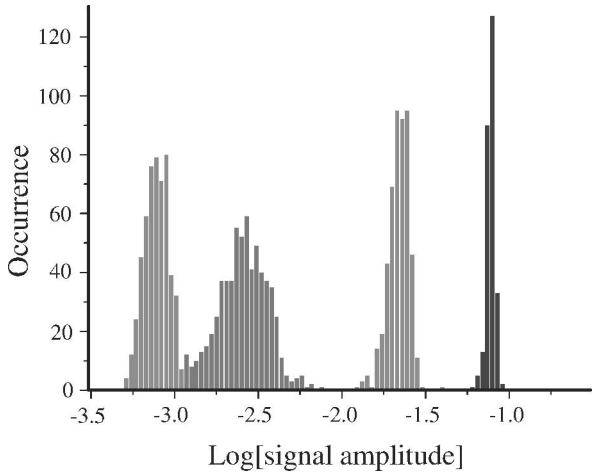

Fig. 5. Measured signal distribution for a sample consisting of a mixture of polystyrene beads of four different sizes. Four distinct peaks can be identified, each corresponding to particles of equal size (starting with the left peak, $R = 25, 50, 100, 175$ nm). Logarithmic scale is used to better visualize the relative size distribution, rather than the absolute values.

Our interferometric sensor can also be applied to detect biological agents. We are currently able to detect single Influenza A X-31 virions in real time, and to discriminate them from other particles of similar size (Fig. 8). Future work is aimed at recognizing different sorts of viruses in a mixture, and separating them subsequently, using standard microfluidic technology.

In order to demonstrate the advantage of the background-free, interferometric detection scheme, we compare the SNR with that of the standard scattering-based detection schemes. According to (10), the maximum normalized differential signal amplitude $(S = 1)$ is obtained when the phase between $\boldsymbol{E}_s$ and $\boldsymbol{E}_r$ (or $\boldsymbol{E}_b$) assumes a value that concentrates all energy on one half of the split detector. This can only happen if the scattered field amplitude is equal to the amplitude of the reference beam or, equivalently, to the amplitude of the backscattered beam, i.e., $P_s = P_b$. For sufficiently strong powers, the SNR becomes

$$\frac{S}{N} = \frac{1}{\theta_{\rm rms}} \sqrt{\frac{P_s}{P_b}}. \tag{15}$$

On the other hand, the maximum SNR in the standard light scattering can be written as

$$\frac{S}{N}_{\rm scattering} = \frac{1}{\eta} \frac{P_s}{P_b} \tag{16}$$

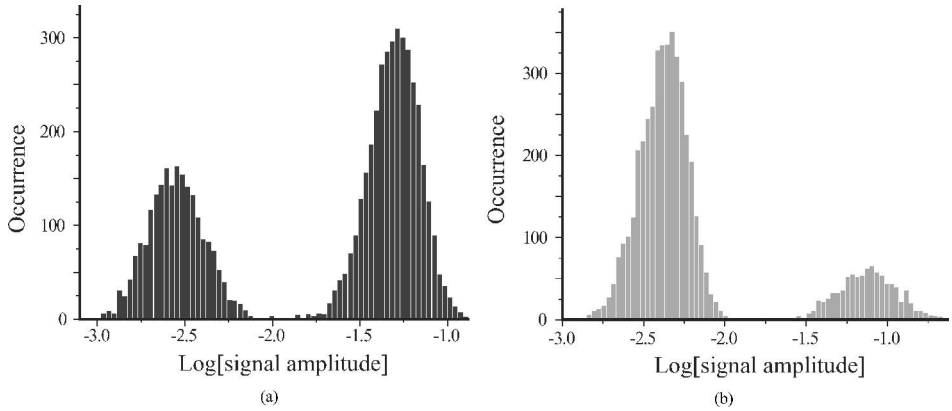

Fig. 6. Signal distributions for a mixture of two particle sizes. (a) Polystyrene beads (15 and 50 nm, *left* and *right peaks*, respectively). (b) Gold spheres (7 and 20 nm, *left* and *right peaks*, respectively). The polarizability of the gold particles is approximately eight times higher than the polarizability of polystyrene beads of similar size. Therefore, the scattered field amplitude for gold is eight times larger than for polystyrene, resulting in a lower detection size limit.

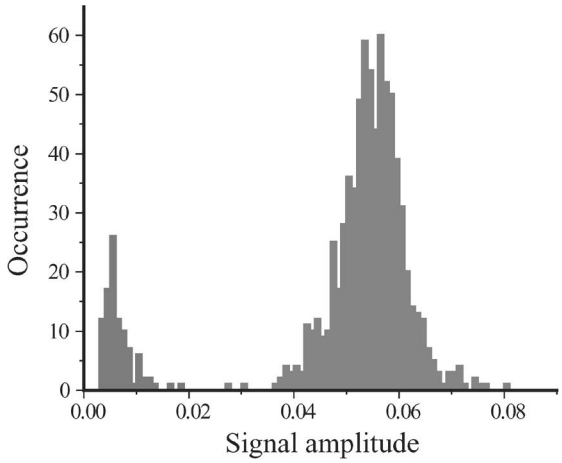

Fig. 7. Signal distribution for a mixture of 50- and 100-nm polystyrene beads. The sample is identical to the one used in the optical force measurements, as shown in Fig. 3. Interferometric detection yields better sensitivity and better resolving power. The *left peak* corresponds to 50-nm particles and the *right peak* corresponds to 100-nm particles.

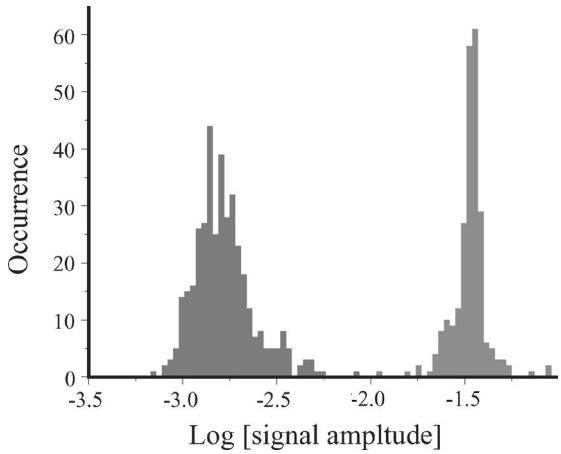

Fig. 8. Histogram of signal amplitudes for a mixture of Influenza A X-31 virus (*left peak*) and 100-nm polystyrene beads. All data sets have been acquired in water with each individual detection event lasting ≈1 ms.

where $\eta = \sqrt{\langle dP \rangle^2}/P$ is the laser power noise. The SNR in our detection scheme is proportional to $\sqrt{P_s/P_b}$, versus P_s/P_b for scattering-based detection, and, therefore, proportional to the third power of the particle size, versus the sixth power of the particle size for scattering-based approaches. The SNR in light scattering depends on the laser power noise that cannot be controlled easily. However, our scheme depends on the angular pointing stability of the laser that can be controlled, for example, by reducing the optical path length. Furthermore, the dimensionless pointing stability coefficient $\theta_{\rm rms}$ for lasers is much smaller (by orders of magnitude) than is typical power noise.

IV. Conclusion

We introduced two optical real-time detection schemes for nanosized particles. In both techniques, the measured signal has a weaker (R^3) particle size dependence compared with the traditional scattering-based detection methods. The first technique is based on measuring the perturbation of the particle motion due to the optical gradient force. The precision of the optical force method is limited by the Brownian motion, which influences the total force acting on the particle and, hence, affects its motion. The precision can be improved by reducing the time it takes for a particle to travel trough the focus and by increasing the laser power. However, the maximum laser power and liquid speed are limited by the heating of the medium and particles, and the detection bandwidth of the position-sensing detector. Nevertheless, the parameters can be optimized for the recognition of the particles of certain size.

The second technique is based on the background-free interferometric detection of the scattered field due to a particle passing through the laser focus. The technique is capable of detecting single nanoparticles in real time with a resolution of 1 ms. The interferometric signal amplitude scales with the third power of the particle size and the use of a split detector ensures the best possible SNR, independent of the laser power noise. In the current configuration, an SNR value of 1 corresponds to detecting a single 10-nm polystyrene particle or a single 5-nm

gold particle. Compared to the optical force detection technique, the interferometric approach possesses much better sensitivity and resolving power. We anticipate that our detection scheme will find applications in a variety of fields such as detection of biowarfare agents (viruses), particle tracking inside cells, or contamination-control of water and air.

REFERENCES

[1] L. A. Broussard, "Biological agents: Weapons of warfare and bioterrorism," *Mol. Diagn.*, vol. 6, no. 4, pp. 323–333, 2001.

[2] M. R. Hillman, "Overview: Cause and prevention in biowarfare and bioterrorism," *Vaccine*, vol. 20, no. 25/26, pp. 3055–3067, 2002.

[3] Center for Desease Control and Prevention. Bioterrorism agents/diseases list. [Online]. Avialble: http://www.bt.cdc.gov/agent/agentlist.asp

[4] W. A. Strohl, H. Rouse, B. D. Fisher, R. A. Harvey, P. C. Champe, and S. P. Champe, *Microbiology*. (Lippincott's Illustrated Reviews Series). Philadelphia, PA: Williams and Wilkins, 2001.

[5] C. A. Tidona, G. Darai, and C. Buuchen-Osmond, *The Springer Index of Viruses*. Berlin, Germany: Springer-Verlag, 2002.

[6] Z. L. Yuan, B. E. Kardynal, R. M. Stevenson, A. J. Shields, C. J. Lobo, K. Cooper, N. S. Beattie, D. A. Ritchie, and M. Pepper, "Electrically driven single-photon source," *Science*, vol. 295, no. 5552, pp. 102–105, 2002.

[7] M. Bruchez, M. Moronne, P. Gin, S. Weiss, and A. P. Alivisatos, "Semiconductor nanocrystals as fluorescent biological labels," *Science*, vol. 281, no. 5385, pp. 2013–2016, 1998.

[8] M. Horisberger and J. Rosset, "Colloidal gold, a useful marker for transmission and scanning electron microscopy," *J. Histochem. Cytochem.*, vol. 25, no. 4, pp. 295–305, 1977.

[9] B. Dragnea, C. Chen, E. Kwak, B. Stein, and C. C. Kao, "Gold nanoparticles as spectroscopic enhancers for in vitro studies on single viruses," *J. Amer. Chem. Soc.*, vol. 125, no. 21, pp. 6374–6375, 2003.

[10] T. Kalkbrenner, M. Ramstein, J. Mlynek, and V. Sandoghdar, "A single gold particle as a probe for apertureless scanning near-field optical microscopy," *J. Microsc.*, vol. 202, pp. 72–76, 2001.

[11] S. Schultz, D. Smith, J. Mock, and D. Schultz, "Single-target molecule detection with nonbleaching multicolor optical immunolabels," *Proc. Nat. Acad. Sci. U.S.A.*, vol. 97, no. 3, pp. 996–1001, 2000.

[12] C. Loo, A. Lin, L. Hirsch, M. H. Lee, J. Barton, N. Halas, J. West, and R. Drezek, "Nanoshell-enabled photonics-based imaging and therapy of cancer," *Technol. Cancer Res. Treat.*, vol. 3, no. 1, pp. 33–40, 2004.

[13] R. Wiese, "Analysis of several fluorescent detector molecules for protein microarray use," *Luminescence*, vol. 18, no. 1, pp. 25–30, 2003.

[14] K. Lindfors, T. Kalkbrenner, P. Stoller, and V. Sandoghdar, "Detection and spectroscopy of gold nanoparticles using supercontinuum white light confocal microscopy," *Phys. Rev. Lett.*, vol. 93, pp. 037401-1–037401-4, 2004.

[15] F. V. Ignatovich and L. Novotny, "Experimental study of nanoparticle detection by optical gradient forces," *Rev. Sci. Instrum.*, vol. 74, no. 12, pp. 5231–5235, 2003.

[16] M. T. Blom, E. Chmela, R. E. Oosterbroek, R. Tijssen, and A. van den Berg, "On-chip hydrodynamic chromatography separation and detection of nanoparticles and biomolecules," *Anal. Chem.*, vol. 75, no. 24, pp. 6761–6768, 2003.

[17] J. Prikulis, F. Svedberg, M. Kall, J. Enger, K. Ramser, M. Goksor, and D. Hanstorp, "Optical spectroscopy of single trapped metal nanoparticles in solution," *Nanoletters*, vol. 4, no. 1, pp. 115–118, 2004.

[18] A. Bouhelier, M. R. Beversluis, and L. Novotny, "Characterization of nanoplasmonic structures by locally excited photoluminescence," *Appl. Phys. Lett.*, vol. 83, no. 24, pp. 5041–5043, 2003.

[19] C. F. Bohren and D. R. Huffman, *Absorption and Scattering of Light by Small Particles*. New York: Wiley, 1983.

[20] L. Fabiny, "Optical particle counters," *Opt. Photon. News*, vol. 9, pp. 34–38, 1998.

[21] M. Kerker, "Light scattering instrumentation for aerosol studies: An historical overview," *Aerosol Sci. Technol.*, vol. 27, no. 4, pp. 522–540, 1997.

[22] A. L. Givan, *Flow Cytometry: First Principles*, 2nd ed. New York: Wiley, 2001.

[23] E. D. Hirleman, "History of development of the phase-doppler particle-sizing velocimeter," *Part. Part. Syst. Char.*, vol. 13, no. 2, pp. 59–67, 1996.

[24] R. Bar-Ziv, A. Meller, T. Tlusty, E. Moses, J. Stavans, and S. Safran, "Localized dynamic light scattering: Probing single particle dynamics at the nanoscale," *Phys. Rev. Lett.*, vol. 78, no. 1, pp. 154–157, 1997.

[25] A. Meller, R. Bar-Ziv, T. Tlusty, E. Moses, J. Stavans, and S. Safran, "Localized dynamic light scattering: A new approach to dynamic measurements in optical microscopy," *Biophys. J.*, vol. 74, no. 3, pp. 1541–1548, 1998.

[26] P. H. McMurry, "The history of condensation nucleus counters," *Aerosol Sci. Technol.*, vol. 33, no. 4, pp. 297–322, 2000.

[27] N. A. Clark, J. H. Lunacek, and G. B. Benedek, "A study of Brownian motion using light scattering," *Am. J. Phys.*, vol. 38, pp. 575–585, 1970.

[28] J. Heitzenberg and R. Charlson, "Design and applications of the integrating nephelometer: A review," *J. Atmos. Ocean. Technol.*, vol. 555, pp. 987–1000, 1996.

[29] J. S. Batchelder and M. A. Taubenblatt, "Measurement of size and refractive index of particles using the complex forward-scattered electromagnetic field," U.S. Patent 5 037 202, Aug. 6, 1991.

[30] J. S. Batchelder, D. M. DeCain, M. A. Taubenblatt, H. K. Wickramasinghe, and C. C. Williams, "Particulate inspection of fluids using interferometric light measurements," U.S. Patent 5 061 070, 1991.

[31] D. Boyer, P. Tamarat, A. Maali, B. Lounis, and M. Orrit, "Photothermal imaging of nanometer-sized metal particles among scatterers," *Science*, vol. 297, no. 5584, pp. 1160–1163, 2002.

[32] A. Ashkin and J. P. Gordon, "Stability of radiation-pressure particle traps—An optical earnshaw theorem," *Opt. Lett.*, vol. 8, no. 10, pp. 511–513, 1983.

[33] A. Ashkin, J. M. Dziedzic, J. E. Bjorkholm, and S. Chu, "Observation of a single-beam gradient force optical trap for dielectric particles," *Opt. Lett.*, vol. 11, pp. 288–290, 1986.

[34] M. J. Lang and S. M. Block, "Laser-based optical tweezers," *Amer. J. Phys.*, vol. 71, pp. 201–215, 2003.

[35] L. Novotny and B. Hecht, *Principles of Nano-Optics*. Cambridge, U.K.: Cambridge Univ. Press, 2006.

[36] F. Gittes and C. F. Schmidt, "Interference model for back-focal-plane displacement detection in optical tweezers," *Opt. Lett.*, vol. 23, pp. 7–9, 1998.

[37] M. S. Z. Kellermayer, S. B. Smith, H. L. Granzier, and C. Bustamante, "Folding-unfolding transitions in single titin molecules characterized with laser tweezers," *Science*, vol. 276, no. 5315, pp. 1112–1116, 1997.

[38] C. Cecconi, E. A. Shank, C. Bustamante, and S. Marqusee, "Direct observation of the three-state folding of a single protein molecule," *Science*, vol. 309, no. 5743, pp. 2057–2060, 2005.

[39] F. V. Ignatovich, A. Hartschuh, and L. Novotny, "Detection of nanoparticles using optical gradient forces," *J. Mod. Opt.*, vol. 50, no. 10, pp. 1509–1520, 2003.

[40] T. S. Stevens and H. J. Cortes, "Electroosmotic propulsion of eluent through silica based chromatographic media," *Anal. Chem.*, vol. 55, no. 8, pp. 1365–1370, 1983.

[41] F. V. Ignatovich and L. Novotny, "Real-time and background-free detection of nanoscale particles," *Phys. Rev. Lett.*, vol. 96, no. 1, pp. 013901-1–013901-4, 2006.

Filipp V. Ignatovich received the M.S. degree in physics from Moscow State University, Moscow, Russia, in 1999. He is currently working toward the Ph.D. degree in optics at the Institute of Optics, University of Rochester, Rochester, NY. He defended his Ph.D. dissertation in September 2006.

In 2001, he joined the Nano-Optics Research Group, Institute of Optics, University of Rochester.

David Topham received the Ph.D. degree in cell and molecular biology from the University of Vermont, Burlington, in 1994.

Currently, he is an Associate Professor of microbiology and immunology in the David H. Smith Center for Vaccine Biology and Immunology, University of Rochester, Rochester, NY, and a Faculty Member at the Center of Excellence in Environmental Health Sciences, University of Rochester.

Lukas Novotny received the Ph.D. degree from the Swiss Federal Institute of Technology (ETH), Zurich, Switzerland, in 1996.

Prior to 1999, he was with the Chemical Structure and Dynamics Group, Pacific Northwest National Laboratory, Richland, WA. In 1999, he joined the faculty of the Institute of Optics, University of Rochester, Rochester, NY, where he is currently the Head of the Nano-Optics Research Group. His current research interests include nanoscale light–matter interactions ranging from questions in solid-state physics to biophysical applications.